High temperature phase transition in SOFC anodes based on $Sr_2MgMoO_{6-\delta}$

D. Marrero-López [a,b,*], J. Peña-Martínez [a], J.C. Ruiz-Morales [a], M.C. Martín-Sedeño [b], P. Núñez [a]

[a] *Departamento de Química Inorgánica, Universidad de La Laguna, 38200-La Laguna, Tenerife, Spain*
[b] *Departamento de Química Inorgánica, Universidad Málaga, 29071-Málaga, Spain*

ARTICLE INFO

ABSTRACT

The double perovskite $Sr_2MgMoO_{6-\delta}$ has been recently reported as an efficient anode material for solid oxide fuel cells (SOFCs). In the present work, this material have been investigated by high temperature X-ray diffraction (XRD), differential scanning calorimetry (DSC) and impedance spectroscopy to further characterise its properties as SOFC anode. DSC and XRD measurements indicate that $Sr_2MgMoO_{6-\delta}$ exhibits a reversible phase transition around 275 °C from triclinic ($I\bar{1}$) with an octahedral tilting distortion to cubic ($Fm\bar{3}m$) without octahedral distortion. This phase transition is continuous with increasing temperature without any sudden cell volume change during the phase transformation. The main effect of the phase transformation is observed in the electrical conductivity with a change in the activation energy at low temperature. La^{3+} and Fe-substituted $Sr_2MgMoO_{6-\delta}$ phases were also investigated, however these materials are unstable under oxidising conditions due to phase segregations above 600 °C.

1. Introduction

solid oxide fuel cells (SOFC) have attracted considerable interest in last few years as the result of several advantages compared to low temperature fuel cells, i.e. the possibility to operate directly on hydrocarbon fuels, greater tolerance to impurities in the fuel, and additionally they do not contain any precious metal, which significantly decreases the cost of these devices [1–3]. However, new anode materials are necessary to produce efficient SOFCs and to overcome many of the problems associated with the state-of-the-art nickel anodes for use in direct reforming SOFCs, such as carbon deposits and sulphur poisoning [4,5]. In this sense, several perovskite type materials have been investigated as potential SOFC anodes, e.g. $La_{1-x}Sr_xCr_{0.5}Mn_{0.5}O_{3-\delta}$ [6] and $La_4Sr_8Ti_{11}Mn_{0.5}Ga_{0.5}O_{37.5-\delta}$ [7], which exhibit high performance operating under H_2 and CH_4 fuels, using yttria stabilised zirconia and doped lanthanum gallate electrolytes [6–8].

Another recently reported SOFC anode is the double perovskite Sr_2MgMoO_6 (SMM) [9,10]. This material has shown excellent performance, possessing high redox stability, and electrocatalytic activity in highly reducing atmosphere using directly methane or natural gas as fuel. Furthermore, modification of the double

perovskite SMM by La^{3+} substitution has been reported to improve the electrocatalytic properties for fuel oxidation [11].

The structure of SMM at room temperature has been initially reported to be tetragonal (space group $I4/m$ [12]) or monoclinic (space group $P2_1/n$ [10]). More recently the structure was studied by Bernuy-Lopez et al. from neutron diffraction data, exhibiting lower symmetry than those previously proposed [13]. This material crystallises at room temperature in the triclinic space group $I\bar{1}$ and adopts a $\sqrt{2} \times \sqrt{2} \times 2$ superstructure of the simple perovskite unit cell due to a tilting distortion of the Mg and Mo-centered octahedra. These authors also reported that SMM presents a limited redox stability range at temperatures above 900 °C due to excessive oxygen deficiency, causing its partial decomposition into a Ruddlesden–Popper phase with a higher Mo:Mg ratio. Nevertheless, several authors have suggested higher stability range for this material up to 1200 °C under hydrogen contained atmosphere [9,10,14].

Several double perovskites with similar composition to SMM, such as Sr_2MWO_6 (M = Ni, Cu, Co, Zn, Mg) [15,16], Sr_2NiMoO_6 [17–19] and Ca_2MgWO_6 [20], undergo phase transitions at high temperatures. Therefore, a phase transition for SMM at high temperature should be expected, although it has not been studied until now. A possible phase transition may affect the electrode-electrolyte interface during fabrication and operation of a SOFC. For example, a first order transition with an abrupt volume change during phase transformation might cause delamination of the electrolyte–anode interface. Therefore, it is essential for practical applications of these materials as SOFC anode to study the possible effects of the phase transformation on the thermal, mechanical and electrical properties.

* Corresponding author at: Departamento de Química Inorgánica, Facultad de Ciencia, Campus de Teatinos, Universidad Málaga, 29071-Málaga, Spain.
Fax: +34 952137534.
E-mail addresses: damarre@uma.es, damarre@ull.es (D. Marrero-López).

In this work, $Sr_2MgMoO_{6-\delta}$, $Sr_{1.5}La_{0.5}MgMoO_{6\pm\delta}$ and $Sr_2Mg_{0.75}Fe_{0.25}MoO_{6-\delta}$ phases were prepared by an alternative freeze-dried precursor method and characterised by high temperature X-ray diffraction (XRD), thermal analysis and impedance spectroscopy. Sr^{2+} was partially substituted by La^{3+} in SMM to enhance the electrocatalytic properties as was found in $Sr_{2-x}La_xMgMoO_{6\pm\delta}$ series with maximum performance values for $x \geqslant 0.5$ [11]. Additionally, Fe with variable oxidation states was introduced to increase the electronic conductivity in these materials.

2. Experimental

As previously reported, the synthesis of SMM by a standard ceramic route is rather complicated due to the segregation of $SrMoO_4$ in air, requiring high sintering temperatures as 1350 °C to obtain a nearly single phase [13,14]. On the contrary, sol–gel and freeze-dried precursor routes allow to reduce the synthesis temperature and to obtain powders with fine grain size. Hence, a modified freeze-dried precursor method, similar to that described elsewhere [14,21], was used to obtain polycrystalline powders of SMM and some substituted phases $Sr_{1.5}La_{0.5}MgMoO_{6\pm\delta}$ (SMM_La$_{0.5}$) and $Sr_2Mg_{0.75}Fe_{0.25}MoO_{6-\delta}$ (SMM_Fe$_{0.25}$).

Starting materials used as reagents were: $Sr(NO_3)_2$ (99.9%), MgO (99.9%), MoO_3 (99.5%), $La(NO_3)_3 6H_2O$ (99.9%) and $Fe(NO_3)_3$ $9H_2O$ (98%) all of them supplied from Aldrich. Metal nitrates, which are generally hygroscopic, were previously studied by thermogravimetric analysis in a TG/DTA Perkin Elmer instrument (mod. Pyris Diamond) to determine the correct cation composition. Cation solutions were prepared separately dissolving metal nitrates in distilled water and MgO and MoO_3 with diluted nitric acid and ammonia, respectively. These solutions were mixed in stoichiometric amounts and ethylenediaminetetraacetic acid (EDTA) (99.5% Aldrich) was added as complexing agent in a 1:1 ligand:metal molar ratio. The solution pH was adjusted to 9 by adding ammonia solution. The volume and cation concentration of the resulting stoichiometric cation solution was 100 ml and 0.2 mol/l of Sr^{2+}. The solutions were flash frozen in liquid nitrogen and then dehydrated in a Heto Lyolab freeze-dryer for 3 days. The dried and amorphous precursor powders were initially precalcined at 300 °C to produce the pirolysis of the organic matter and then calcined at 600 °C for 5 h to remove the residual organic species. The powders were finally calcined in a tubular furnace flowing dry 5% H_2–Ar between 950 and 1000 °C for 10 h.

XRD patterns were obtained from a PANalytical X'Pert Pro automated diffractometer, equipped with a Ge(111) primary monochromator and an X'celerator detector. The scans were collected in high resolution mode in the 2θ range (10–100°) with 0.016° step for 2–4 h. High-temperature XRD studies were performed in air, using an Anton Paar HTK-16 Camera, ranging from RT to 600 °C. Rietveld refinements of the XRD patterns were performed using FULLPROF and WinPlotr software [22,23]. The usual profile parameters (scale factors, background coefficients, zero-points, half-width, pseudo-Voigt, asymmetry parameters for the peak-shape, atomic positions and isotropic temperature factors) were refined. The occupation numbers were not refined.

Differential scanning calorimetry (DSC) analysis were recorded with a power-compensation Perkin Elmer Instruments (Pyris Diamond series) in air between room temperature (RT) and 450 °C at heating/cooling rate of 20 °C/min. The powders ($\sim$150 mg) were deposited in Al crucibles and hermetic closed under pressure.

For the electrical characterisation, ceramic pellets were prepared by pressing the oxide powders into disks of 5 mm of diameter and 4 mm of thickness at 125 MPa. The resulting pellets were sintered at 1200 °C in air for 5 h, reaching relative densities

higher than 90%. Pt electrodes were painted on each side of the pellet as current collectors. The overall electrical conductivity was determined by impedance spectroscopy under air and wet 5%H_2–Ar, using a 1260 Solartron frequency response analyser on cooling and heating from 950 to 250 °C. The spectra were fitted by equivalent circuits using the ZView program to obtain the electrical resistance and conductivity values of the samples [24]. Additional experimental details are reported elsewhere [14,21].

3. Results and discussions

3.1. Thermal analysis

The stability of SMM under oxidising and reducing conditions was studied in a previous work [14]. This material seems to be stable in both air and dry 5% H_2–Ar up to 1200 °C. Thermogravimetric analysis confirmed that oxidised SMM sample does not exhibit appreciable weight loss between RT and 700 °C. The reduction of SMM is small even under strongly reducing conditions, experimenting an oxygen loss of about 0.15 oxygen atoms per formula unit after reduction under dry 5% H_2–Ar at 1200 °C for 24 h. On the other hand, the reoxidation of the pre-reduced phase begins above 500 °C. It should be also commented that no significant structural changes are found between the reduced and oxidised phases in agreement with previous works [13,14].

The DSC curves for SMM show a weak endothermic transformation on heating which is reversible as an exothermic peak during the cooling process seems to indicate (Fig. 1). On heating, the onset of the endothermic change occurs at 243 °C and reaches a maximum at about 275 °C. On cooling, the onset of the peak is shifted to somewhat higher temperatures (about 273 °C) and the minimum peak is found at 255 °C. These differences during the heating and cooling processes can be attributed to hysteresis phenomena and also kinetic effects due to the fast heating/cooling
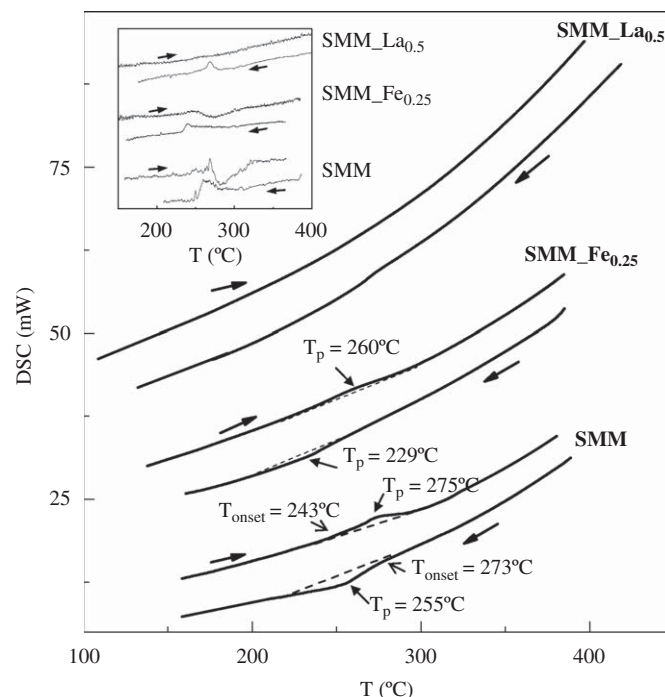
Fig. 1. DSC curves showing the reversible phase transformation for $Sr_2MgMoO_{6-\delta}$ (SMM), $Sr_2Mg_{0.75}Fe_{0.25}MoO_{6-\delta}$ (SMM_Fe$_{0.25}$) and $Sr_{1.5}La_{0.5}MgMoO_{6-\delta}$ (SMM_La$_{0.5}$). The inset shows the derivate of the DSC curves.

rate used (20 °C/min). It has to be considered that a fast heating/cooling rate was used to enhance the sensitivity and to identify the weak transformation. The power-compensation DSC equipment is formed by two small separated furnaces for the sample and the reference allowing heating rates as high as 200 °C/min, however fast heating/cooling rates shift the thermal transformation peak at higher and lower temperatures, respectively. Thus, the hysteric phenomena observed in the DSC curves could be associated to the heating rate used. On the other hand, the reversible thermal transformation was observed in both the oxidised and reduced phases.

The enthalpy change at the phase transition ($\Delta H \sim 65$ J/mol) was calculated by numerical integration of the recorded DSC curves, after the correction for the calorimetric base line, using the relationship:

$$\Delta H = \int \frac{Q}{\beta} \, dt$$

where Q is the heat flow, β the heating rate, and t the time.

A thermal change is also visible in SMM_Fe$_{0.25}$ sample, although the enthalpy change is lower than that for SMM, whereas this is not easily detectable for SMM_La$_{0.5}$ sample. However, an analysis of the data in terms of the derivation of the DSC curves (inset Fig. 1) reveals a small peak for SMM_La$_{0.5}$, which may be related to a phase change.

3.2. Structural characterisation at high temperature

3.2.1. Non-substituted SMM

As previously mentioned, the structure of SMM has been reported to be tetragonal (s.g. I4/m), monoclinic (s.g. $P2_1/n$) and/or triclinic (s.g. $I\bar{1}$). In the present work, the Rietveld refinements for SMM at RT were performed in tetragonal I4/m and triclinic $I\bar{1}$ models. The results considering the tetragonal and the triclinic structural models are shown in Fig. 2a and b, respectively, and the unit cell parameters are listed in Table 1. Due to the low accuracy in the determination of the oxygen atoms position from XRD data compared to the results previously reported by Bernuy-Lopez et al. [13] from neutron diffraction, the structural parameters (atomic position, thermal factor and selected interatomic distances) are given as supplementary material in Table 2. The cell parameters indicated that SMM presents a very low triclinic distortion and non appreciable differences are observed in the Rietveld refinements from XRD data when refined in a triclinic or a tetragonal cell. The R-factors are even similar (supplementary material). This is not surprising, because the difference between both structural models implies only displacements of some oxygen atoms from ideal positions as it was proposed by Bernuy-Lopez et al. [13]. One can also observe that the accuracy in the determination of the cell parameters in s.g. $I\bar{1}$ is somewhat lower compared to s.g. I4/m. The refinement convergence in the triclinic space group was somewhat complicated and the thermal factors were fixed, while they were freely refined in s.g I4/m. Furthermore, the uncertainty in the oxygen positions is significant due to the dominant scattering power of the heavy cations compared to the oxygen atoms as previously commented. For these reasons the results between tetragonal and triclinic models seems to be similar using XRD data. Thus, neutron diffraction is a more appropriate technique to study the structure of this material at low temperature [13]. Another issue to be considered is that the different synthesis methods and annealing temperatures used may affect the structure of this material. In this sense, samples obtained by freeze-dried precursor were synthesised at much lower temperature (1000 °C) than those prepared by conventional solid state reaction (1350 °C) [13] and sol-gel (1200 °C) [10]. A
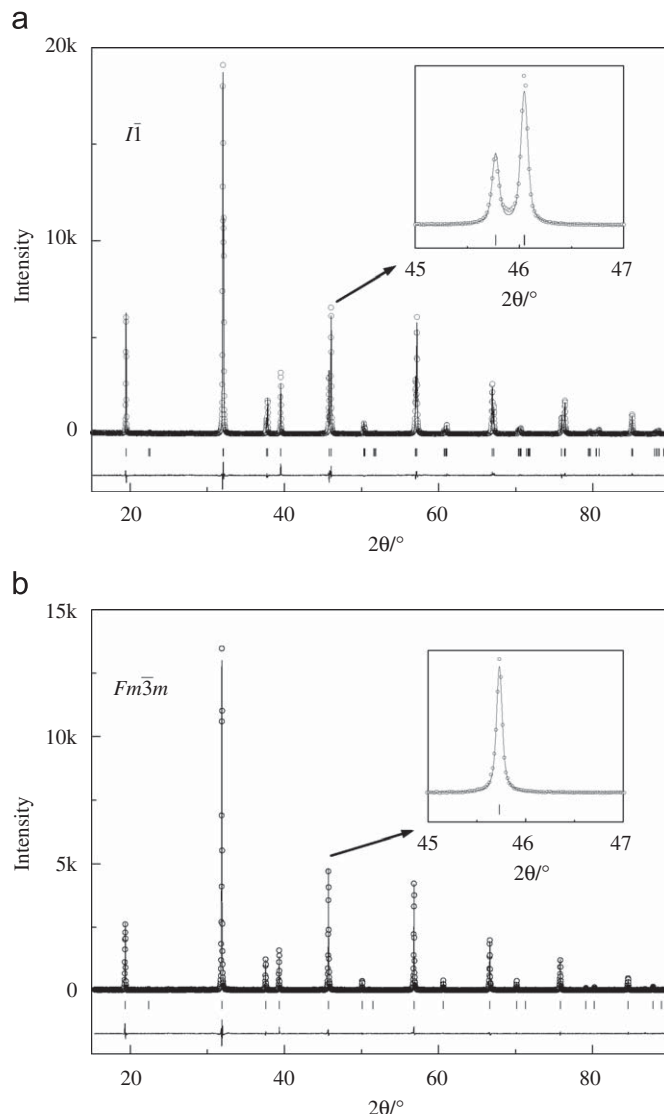

Fig. 2. Rietveld refinement for Sr$_2$MgMoO$_{6-\delta}$ in the space groups (a) triclinic $I\bar{1}$ at room temperature and (b) cubic $Fm\bar{3}m$ at 500 °C. Ticks marks indicate the allowed Bragg reflections, experimental (circles), calculated (continuous line), and difference profiles. The insets show the fitting of some diffraction peaks in the 2θ region near 46°.

small molybdenum volatilisation at high synthesis temperatures might produce changes in the structure.

Fig. 3 shows the thermal evolution of XRD patterns collected between RT and 600 °C, revealing noticeable changes in the patterns, especially in the high 2θ range. Inspection of the diffraction peak around 45° shows two reflexions at low temperature, which coalesce gradually as the temperature increases into a single reflection, indicating less lattice distortion and the tendency to higher symmetric structure. Moreover, the apparent peak intensity increases as the peak overlap increases from RT to 275 °C. The reason is that the unit cell becomes more pseudocubic as the temperature increases and above 275 °C is cubic as also occurs in other double perovskites, such as Sr$_2$NiMoO$_6$ [16]. No other structural changes are observed above 275 °C. The high temperature XRD patterns were refined as an ordered cubic double perovskite with space group $Fm\bar{3}m$ [16,17]. The Rietveld refinement for the pattern at 500 °C is shown in Fig. 2b and the corresponding structural parameters and selected

Table 1
Lattice cell parameters for the different phases

Composition	s.g.	a (Å)	b (Å)	c (Å)	α (°)	β (°)	γ (°)
Sr_2MgMoO_6 (RT)	$I4/m$	5.57446(4)	–	7.92304(6)	–	–	–
Sr_2MgMoO_6 (RT)	$I\bar{1}$	5.5702(1)	5.5709(2)	7.9228(1)	89.962(2)	90.011(9)	90.003(7)
Sr_2MgMoO_6(500 °C)	$Fm\bar{3}m$	7.9308(8)	–	–	–	–	–
$Sr_2Mg_{0.75}Fe_{0.25}MoO_6$ (RT)	$I4/m$	5.5669(1)	–	7.9128(1)	–	–	–
$Sr_{1.5}La_{0.5}MgMoO_6$ (RT)	$I\bar{1}$	5.5912(2)	5.5925(2)	7.9170(1)	89.834(4)	90.189(4)	90.279(1)
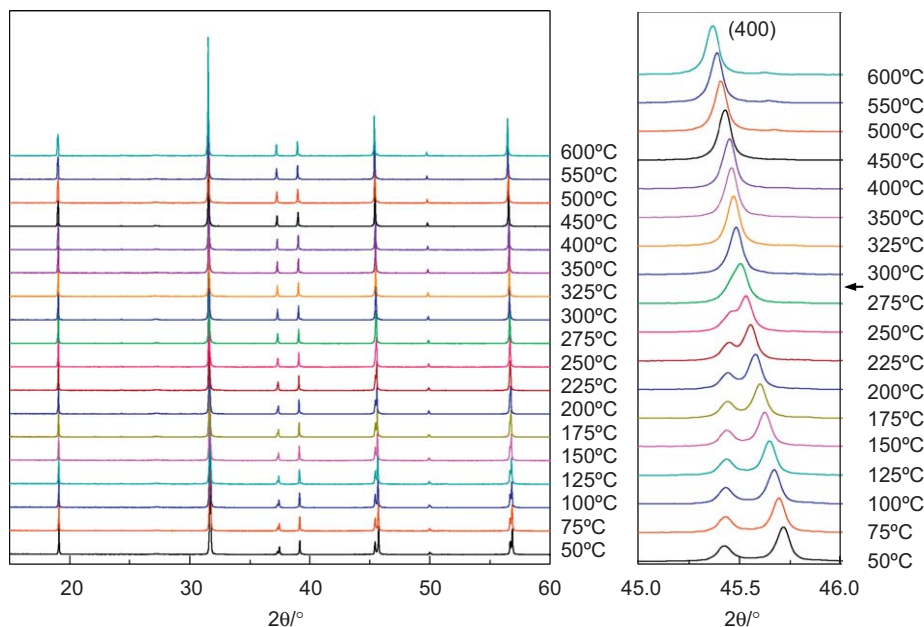
Fig. 3. Thermal evolution of the XRD patterns for $Sr_2MgMoO_{6-\delta}$ between RT and 600 °C. The details of selected 2θ ranges are also displayed.

interatomic distances are listed as supplementary material in Table 2.

The structure representation is shown in Fig. 4. One can notice the absence of octahedral tilting distortion of the cubic phase at 500 °C compared to the triclinic phase at RT.

The temperature dependence of the lattice parameters is shown in Fig. 5, where the a parameter has been divided by $\sqrt{2}$ for comparison. The low temperature patterns were indexed in a triclinic cell, while the high temperature patterns were indexed in a cubic cell. As can be observed the a and b parameters, with similar values, increase with the temperature, while that the c-axis parameter decreases slightly. The more rapid change in the (a,b)-axis is correlated to a change in the octahedral tilting, which does not affect the c-axis in the limit of rigid octahedra. The thermal dependence of the normalised unit cell volume is given in Fig. 6. A linear trend is observed between RT and 600 °C, minimising a possible mechanical thermal stress during the phase transformation. The low enthalpy change and the linear dependence of the cell volume with the temperature suggest a predominant second order type phase transition for SMM at 275 °C.

The linear thermal expansion coefficient (α_L) has been calculated from the volumetric thermal expansion coefficient (α_V) from the relation ($\alpha_V = 3\alpha_L$). The obtained value of linear thermal expansion coefficient (TEC) for SMM is $(11.70\pm0.001)\times 10^{-6}\,K^{-1}$ in the temperature range RT-600 °C. This TEC value is similar to that previously reported by Huang et al. [10] from dilatometric measurements ($11.7\times 10^{-6}\,K^{-1}$ in the range 110–360 °C and $12.7\times 10^{-6}\,K^{-1}$ in the

range 418–800 °C). It should be noted that the slight different TEC values found by Huang et al. between the high and low temperature range can be associated to the phase transition, which was not considered by these authors.

In addition, the TEC value of SMM is comparable to the standard solid electrolytes used in SOFCs: YSZ ($10.8\times 10^{-6}\,K^{-1}$), $Ce_{0.8}Gd_{0.2}O_{1.9}$ ($12.5\times 10^{-6}\,K^{-1}$) and $La_{0.8}Sr_{0.2}Ga_{0.8}Mg_{0.2}O_{2.8}$ ($11.4\times 10^{-6}\,K^{-1}$) [1]. This presumes a good mechanical compatibility between SMM and these electrolytes.

3.2.2. Substituted phases

The Rietveld refinements for two substituted samples with composition $Sr_2Mg_{0.75}Fe_{0.25}MoO_{6-\delta}$ (SMM_Fe$_{0.25}$) and $Sr_{1.5}La_{0.5}MgMoO_{6\pm\delta}$ (SMM_La$_{0.5}$) are shown in Fig. 7a and b.

Rietveld refinements for SMM_Fe$_{0.25}$ were performed in a tetragonal ($I4/m$) and triclinic ($I\bar{1}$) space groups. The inset of Fig. 7a shows the fitting of the XRD pattern in a selected 2θ range around 67°. As can be observed the fitting results are similar and the lattice cell parameters obtained in both models suggest that the unit cell can be considered as tetragonal and similar to $Sr_2(Fe,Ni)MoO_6$ [17,18,25]. Since the oxygen parameters can not be refined correctly using XRD data, we can not rule out that the real structure could be triclinic as occurs with non-substituted $Sr_2MgMoO_{6\pm\delta}$ from neutron diffraction data. Atomic parameter and selected interatomic distances are given as supplementary material in Table 3.

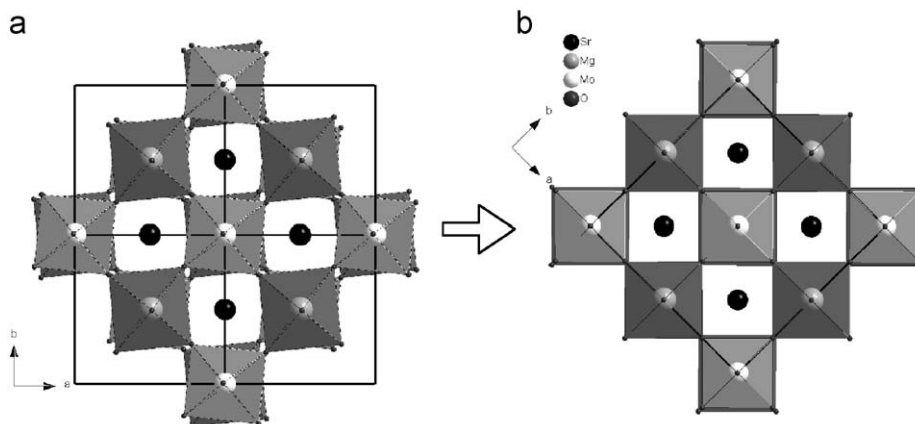On the other hand, refinements for SMM_La$_{0.5}$ considering a tetragonal cell (s.g. $I4/m$ and $I4/mmm$) were unsatisfactory.

Fig. 4. Structure of $Sr_2MgMoO_{6-\delta}$ viewed along the c-axis in the space group: (a) $I\bar{1}$ at room temperature and (b) $Fm\bar{3}m$ at 500 °C.

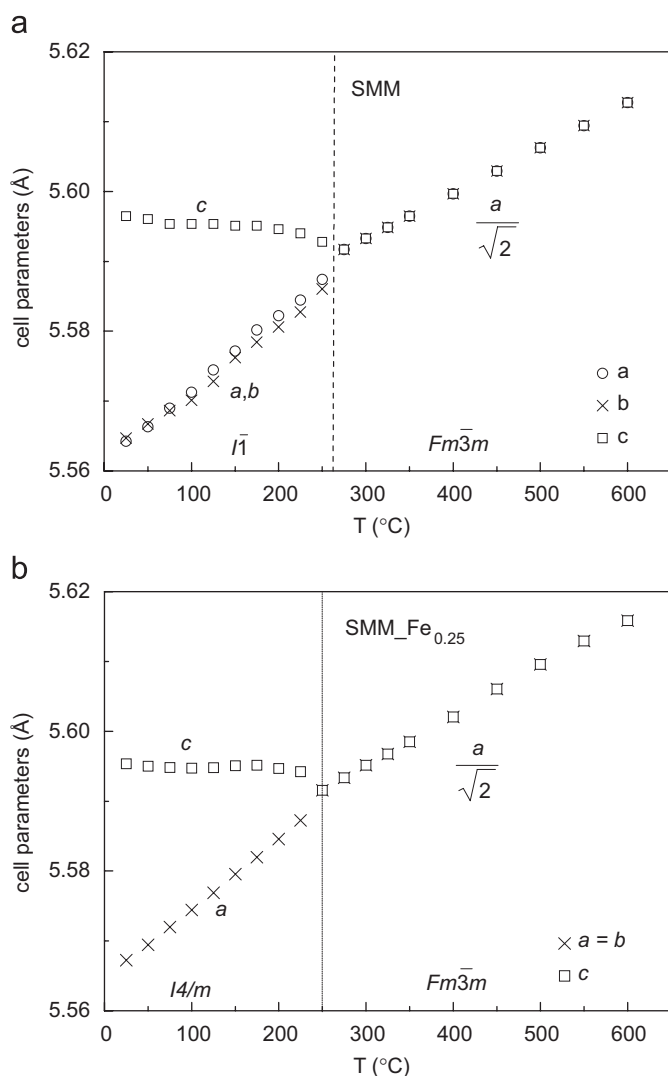**Fig. 5.** Temperature dependence of the lattice parameters for: (a) $Sr_2MgMoO_{6-\delta}$ and (b) $Sr_2Mg_{0.75}Fe_{0.25}MoO_{6-\delta}$.

Fig. 6. Thermal evolution of cell volume for $Sr_2MgMoO_{6-\delta}$ (SMM), $Sr_2Mg_{0.75}Fe_{0.25}MoO_{6-\delta}$ (SMM_Fe$_{0.25}$) and $Sr_{1.5}La_{0.5}MgMoO_{6-\delta}$ (SMM_La$_{0.5}$).

the pattern, but no convergence was achieved when atomic parameters were refined. The refinement in the monoclinic structure with space group $P2_1/n$, observed in many double perovskite compounds [15,16,19], gave a reasonable good fit of the diffraction profile and no unindexed peaks or large differences between the experimental and calculated intensities were observed. In addition, the agreement factors of the refinement in $P2_1/n$ ($R_p = 10.3\%$, $R_{wp} = 11.2\%$, $R_{exp} = 6.47\%$, $R_F = 6.55\%$, $R_B = 3.0\%$) were slightly larger compared to the triclinic model $I\bar{1}$ ($R_p = 8.5\%$, $R_{wp} = 8.5\%$, $R_{exp} = 5.8\%$, $R_F = 3.82\%$, $R_B = 2.9\%$). Thus, the SMM_La$_{0.5}$ phase seems to be fitted better using the triclinic model.

The atomic position and some selected interatomic distances are listed as supplementary material in Table 3.

The variation with the temperature of a selected region of the XRD patterns for SMM_Fe$_{0.25}$ and SMM_La$_{0.5}$ are shown in Fig. 7c and d. In the case of SMM_Fe$_{0.25}$ (Fig. 7c) the examination of the diffraction peaks in the 2θ range around 45° shows a clear doublet, that trend to collapse as a single reflection, indicating that the structure becomes cubic as the temperature increases as occurs with SMM. The XRD patterns for SMM_La$_{0.5}$ show peak splitting at low temperature; however a substantial peak broadening is observed as the temperature increases, which complicate the structural analysis. The stability of this material

These models could not account for the splitting of some diffraction peaks as can be observed in the inset of Fig. 7b. Different structural models proposed for double perovskite compounds and also proposed previously by Bernuy-Lopez et al. for SMM were investigated [13,15,16,19]. The refinement based on $Pmm2$ and $Immm$ space groups indexed all the diffraction peaks of
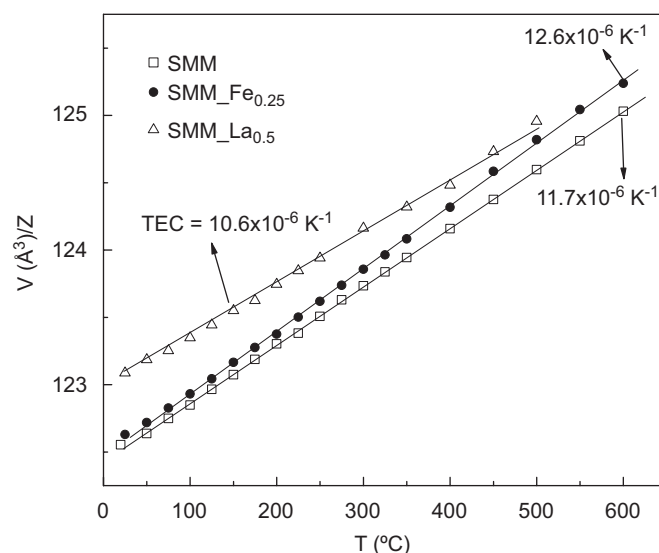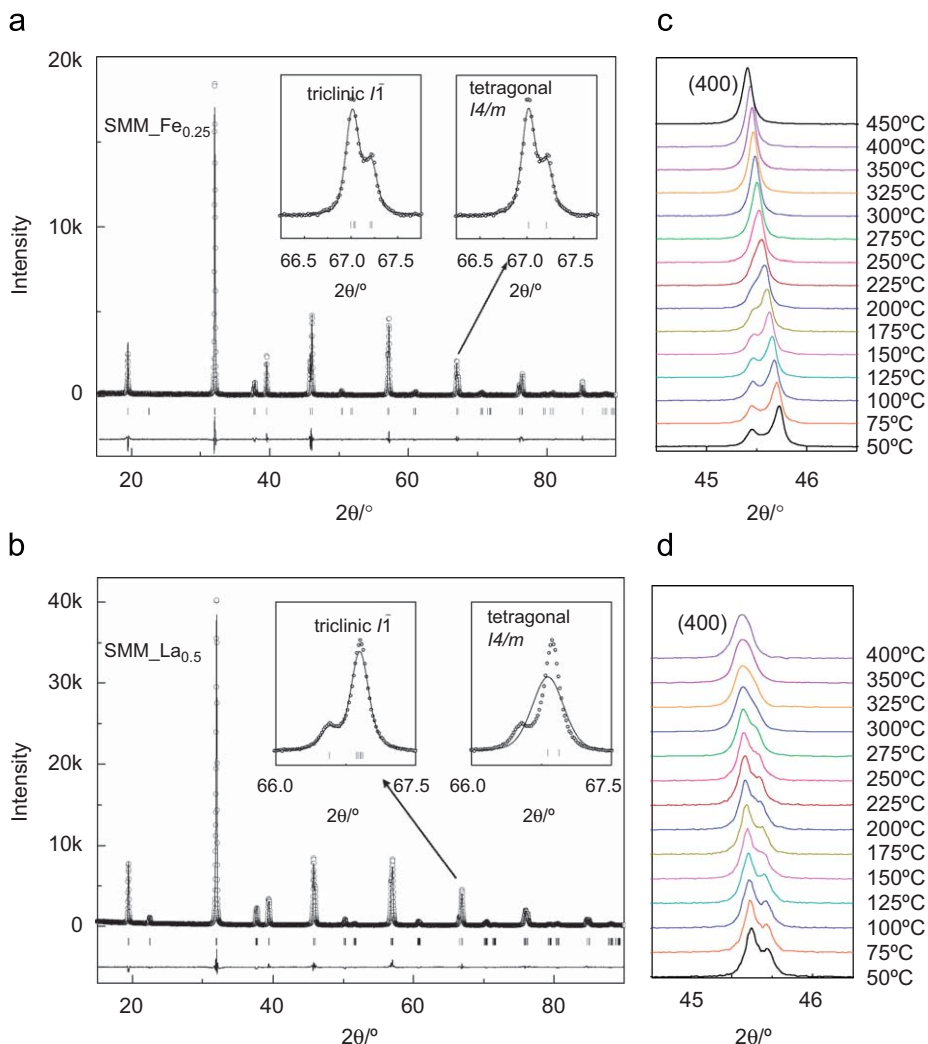
Fig. 7. Rietveld refinement at room temperature for: (a) $Sr_2Mg_{0.75}Fe_{0.25}MoO_{6-\delta}$ in the space groups $I4/m$ and (b) $Sr_{1.5}La_{0.5}MgMoO_{6-\delta}$ in the space groups $I\bar{1}$. The insets show the fitting results considering a tetragonal and triclinic cell of some selected diffraction peaks around 67°. Thermal evolution of a selected 2θ range around 45° of the XRD patterns for: (c) SMM_Fe$_{0.25}$ and (d) SMM_La$_{0.5}$.

was studied by annealing the sample in air conditions between 700 and 1000 °C for 5 h. The XRD patterns (Fig. 8) indicate a partial decomposition of the double perovskite structure with the formation of $SrMoO_4$ and segregation of La_2O_3. A similar behaviour was found for SMM_Fe$_{0.25}$, although only $SrMoO_4$ is observed as secondary phases after calcination above 700 °C. Despite this material would operate as a SOFC anode under reducing conditions, where no degradation occurs. This degradation under oxidising conditions is a clear drawback for practical applications, because the SOFC fabrication process is carried out generally in air conditions. Moreover, the segregation of $SrMoO_4$, which is insulating, may modify the transport properties of the anode. Taking into account that La-doped $Sr_2MgMoO_{6-\delta}$ contains a mixture of Mo^{6+} and Mo^{5+} cations, necessary to compensate the charge when Sr^{2+} is substituted by La^{3+}. The oxidation of Mo^{5+} to Mo^{6+} under oxidising conditions seems to be the reason of the low stability of these materials in air. Notice that the synthesis was carried out under reducing conditions. In fact, the samples prepared in air up to 1300 °C showed impurities of $SrMoO_4$ and La_2O_3.

The temperature dependence of lattice cell parameters for SMM_Fe$_{0.25}$ (Fig. 5b) shows that the c-axis decreases smoothly with the temperature, whilst the a-axis increases as well as non-substituted SMM sample.
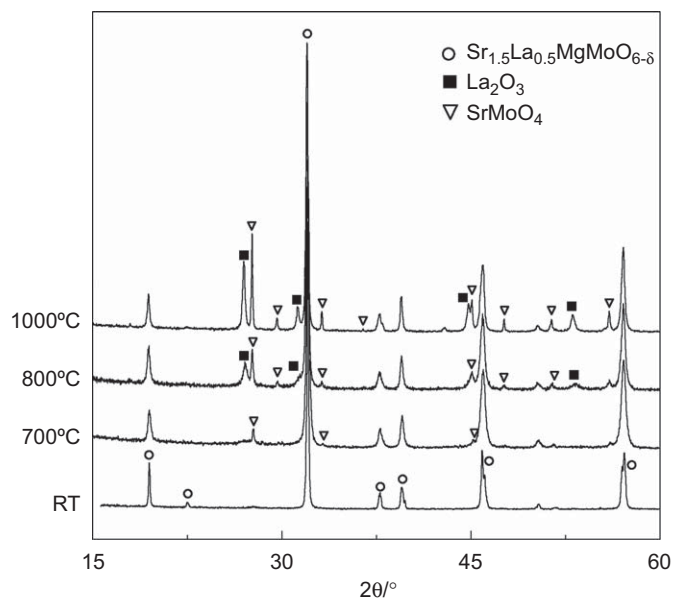
Fig. 8. Variation of the XRD patterns for $Sr_{1.5}La_{0.5}MgMoO_{6-\delta}$ as a function of the annealing temperature in air conditions, showing phase segregations above 700 °C.
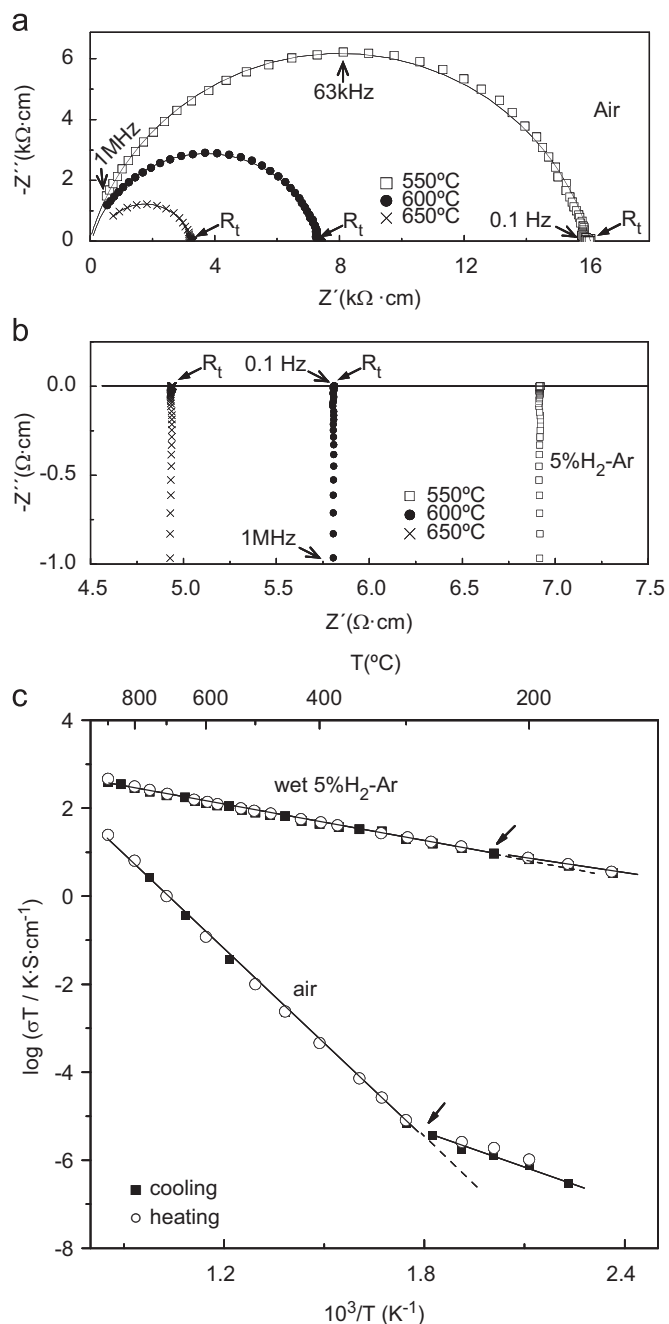
Fig. 9. Impedance spectra in: (a) air and (b) wet 5% H$_2$–Ar for Sr$_2$MgMoO$_{6-\delta}$. (c) Arrhenius plots of the overall conductivity for Sr$_2$MgMoO$_{6-\delta}$ in air and 5% H$_2$–Ar during the heating and cooling process.

The variation of the cell volume with the temperature is shown in Fig. 6 and the estimated TEC values are 12.6×10^{-6} K^{-1} for SMM_Fe$_{0.25}$ and 10.6×10^{-6} K^{-1} for SMM_La$_{0.5}$ between RT and 600 °C. As can be observed, La-substitution in SMM produces a decrease of the TEC value compared to non-substituted SMM. Fe-substituted phase has higher TEC value, possible due to Fe reduction as the temperature increases.

3.3. Electrical characterisation

The electrical characterisation was carried out by impedance spectroscopy using dense ceramic pellets sintered in air. Due to the low stability of SMM_La$_{0.5}$ and SMM_Fe$_{0.5}$, only SMM sample was electrically characterised.

The impedance spectra in air (Fig. 9a) consist in a depressed arc, which were adjusted with an equivalent circuit formed by a resistance and a pseudocapacitance in parallel. The resistance R_t values obtained with the fitting were used to determine the overall conductivity: $\sigma = L/(SR_t)$, where L and S are the sample thickness and electrode area, respectively. In a diluted hydrogen atmosphere, only inductive effects are observed in the impedance spectra (Fig. 9b), indicating predominant electronic conductivity. In this case, the overall material resistance was obtained from the low frequency interception with the Z'-axis.

The Arrhenius plots of the overall conductivity for SMM in air and wet 5% H$_2$–Ar during the heating and cooling processes is shown in Fig. 9c. A change in the Arrhenius behaviour is observed above the phase transition temperature, which is more significant in air. The values of activation energies were obtained from the slopes of the Arrhenius plots. In air the phase transition is found around 275 °C, similar to those found by DSC and XRD measurements. The activation energies are 0.52 ± 0.03 and 1.43 ± 0.01 eV in the low and high temperature range, respectively. Non-appreciable hysteresis phenomena are observed during the heating and cooling processes. In reducing atmosphere (wet 5% H$_2$–Ar) only a slight slope change in the Arrhenius plot is detectable with very similar activation energies, i.e. 0.270 ± 0.002 and 0.250 ± 0.003 eV in the high and low temperature range, respectively.

In summary, Sr$_2$MgMoO$_{6-\delta}$ exhibits a structural phase transition from triclinic ($I\bar{1}$) to cubic ($Fm\bar{3}m$), like other double perovskites, such as Sr$_2$NiMoO$_6$. This phase transition is associated to a rotation of the MoO$_6$ and MgO$_6$ octahedra. The phase transformation is detectable by DSC analysis at 275 °C, displaying a very low enthalpy change, about 65 J/mol. A continuous cell volume increase was observed during the phase transformation, reducing any possible thermal stresses during the material operation in a SOFC. The Arrhenius plot of the overall conductivity showed a change of activation energy above the phase transition temperature, which is more visible under air atmosphere. Hence, this phase transition is non a limiting factor for the practical application of non-substituted Sr$_2$MgMoO$_{6-\delta}$ as SOFC anode, although more detailed studies on the stability during long term operation and chemical compatibility with the different SOFC components are required. In fact, molybdenum might easily diffuse into the other cell components, leading to the formation of different reaction products, as it has been observed in other molybdenum contained materials, such as the solid electrolyte La$_2$Mo$_2$O$_9$ [26]. These studies are actually in progress.

La-substituted Sr$_2$MgMoO$_{6-\delta}$, which has been recently considered as a more efficient anode material compared to Sr$_2$MgMoO$_{6-\delta}$, exhibits also a phase transformation at high temperature. However, the stability studies indicated that substituted phases decompose under oxidising conditions, being a serious drawback for practical applications of these materials in a SOFC.

Acknowledgments

Appendix A. Supplementary material

Supplementary data associated with this article can be found in the online version at 10.1016/j.jssc.2009.01.018.

References

[1] N.Q. Minh, T. Takahashi, Science and Technology of Ceramic Fuel Cells, Elsevier Science, Amsterdam, Netherlands, 1995.

[2] S.C. Singhal, K. Kendall, High Temperature Solid Oxide Fuel Cells: Fundamental, Design and Applications, Elservier, Oxford, 2004.

[3] B.C.H. Steele, A. Heinzel, Nature 414 (2001) 345.

[4] A. Atkinson, S.A. Barnett, R.J. Gorte, J.T.S. Irvine, A.J. McEvoy, M. Mogensen, S.C. Singhal, J. Vohs, Nat. Mater. 3 (2004) 17.

[5] J.B. Goodenough, Y.-H. Huang, J. Power Sources 173 (2007) 1.

[6] S. Tao, J.T.S. Irvine, Nat. Mater. 2 (2003) 320.

[7] J.C. Ruiz-Morales, J. Canales-Vázquez, C. Savaniu, D. Marrero-López, W. Zhou, J.T.S. Irvine, Nature 439 (2006) 568.

[8] J. Peña-Martinez, D. Marrero-López, J.C. Ruiz-Morales, C. Savaniu, P. Núñez, J.T.S. Irvine, Chem. Mater. 18 (2006) 1001.

[9] Y.H. Huang, R.I. Dass, Z.L. Xing, J.B. Goodenough, Science 312 (2006) 254.

[10] Y.H. Huang, R.I. Dass, J.C. Denyszyn, J.B. Goodenough, J. Electrochem. Soc. 153 (2006) A1266.

[11] Y. Ji, Y.H. Huang, J.R. Ying, J.B. Goodenough, Electrochem. Comm. 9 (2007) 1881.

[12] F. Sher, A. Venimadhav, M.G. Blamire, B. Dabrowski, S. Kolesnik, P.J. Attfiel, Solid State Sci. 7 (2005) 912.

[13] C. Bernuy-Lopez, M. Allix, C.A. Bridges, J.B. Claridge, M.J. Rosseinsky, Chem. Mater. 19 (2007) 1035.

[14] D. Marrero-López, J. Peña-Martínez, J.C. Ruiz-Morales, D. Pérez-Coll, M.A.G. Aranda, P. Núñez, Mater. Res. Bull. 8–9 (2008) 2441.

[15] M. Gateshki, J.M. Igartua, E. Hernández-Bocanegra, J. Phys: Condens. Matter 15 (2003) 6199.

[16] M. Gateshki, J.M. Igartua, J. Phys: Condens. Matter 16 (2004) 6649.

[17] A.K. Eriksson, S.-G. Eriksson, S.A. Ivanov, C.S. Knee, J. Eriken, H. Rundlöf, M. Tseggai, Mater. Res. Bull. 41 (2006) 144.

[18] M.J. Martinez-Lope, J.A. Alonso, M.T. Casais, Eur. J. Inorg. Chem. 15 (2003) 2839.

[19] M.W. Lufaso, R.B. Macquart, Y. Lee, T. Vogt, H.-C. Zur Loye, J. Phys: Condens. Matter 18 (2006) 8761–8780.

[20] S.J. Patwe, S.N. Achary, M.D. Mathews, A.K. Tyagi, Mater. Chem. Phys. 98 (2006) 486.

[21] D. Marrero-López, J. Peña-Martínez, D. Pérez-Coll, P. Núñez, J. Alloys Compd. 422 (2006) 249.

[22] J. Rodríguez-Carvajal, Phys. B: Condens. Matter 192 (1993) 55.

[23] T. Roisnel, J. Rodríguez-Carvajal, WinPLOTR, a Graphic Tool for Powder Diffraction, Laboratoire Léon Brillouin-LCSI, France, 2005.

[24] D. Johnson, ZView: a Software Program for IES Analysis, Version 2.8, Scribner Associates, Inc., Southern Pines, NC, 2002.

[25] K.L. Kobayashi, T. Kimura, H. Sawada, K. Terakura, Y. Tokura, Nature 395 (1998) 677.

[26] D. Marrero-López, J. Peña-Martínez, J.C. Ruiz-Morales, D. Pérez-Coll, M.C. Martín-Sedeño, P. Núñez, Solid State Ionics 178 (2007) 1366.